Room-Temperature Ammonia Sensor Based on Cationic Surfactant-Assisted Nanocrystalline CuO

Ratish K. Bedi[†] **and Iqbal Singh***[,‡]

Material Science laboratory, Department of Physics, Guru Nanak Dev University, Amritsar 143005, Punjab, India, and P.G. Department of Physics, Khalsa College, Amritsar 143005, Punjab, India

ABSTRACT CuO nanocrystalline powder was synthesized by a sol−gel auto combustion route with different amounts of the cetyltrimethylammonium bromide (CTAB) used as cationic surfactant. The samples were characterized by XRD, FESEM, and TEM techniques. The electrical properties of the samples without and with different CTAB concentration and the response to ammonia gas at room temperature have been investigated. The CTAB appears to influence the morphology and the properties of CuO powder. The lattice constant values of the samples indicate monoclinic structure. TEM indicate the crystallite size around 7 nm for the CuO with 0.5M CTAB. The addition of surfactant results in an increase in the response of CuO thick films for ammonia at room temperature.

KEYWORDS: nanoparticles • auto combustion • sensor • strain • semiconductor

INTRODUCTION

Metal oxide nanostructures are considered as building blocks for chemical sensing applications (1−3). The shape and size are important factors in determining the structural, physical, and chemical properties of nanoparticles. Different morphological structures of nanoparticles have different electronic, optical, and magnetic properties. The large surface to volume ratio facilitates their applications as gas sensor and in many fields such as industry, mining, traffic safety, etc. (4, 5).

CuO is a black solid acting as an electric insulator with direct band gap of 1.36 eV, which makes it a promising material for use in solar cells (6, 7), as a catalyst (8), and for gas sensing device applications (9). A variety of CuO structures have been fabricated using different synthesis techniques (9−13). The reports suggest that higher temperature, longer reaction time, and sophisticated instruments are required for the growth of CuO nanostructures. There is a need to develop a simple, easy and effective method to synthesize the complex CuO nanostructures in large quantity.

CTAB has been widely used as a cationic surfactant for the synthesis of inorganic materials with a controlled shape and size (14, 15). The addition of surfactant reduces the surface tension of the precursor solution, facilitating nucleation and the formation of new phases. Cationic surfactant molecules composed from a hydrophilic head and a hydrophobic tail into precursor of sol−gel autocombustion method results the formation of reverse micelles in the gel. Hydrocarbonic tail can play the role of fuel in the combustion process, whereas the formation of reverse micelles control the growth and the distance between the particles and hence agglomeration.

In the present work, CuO nanostructures were synthesized using cetyltrimethyl ammonium bromide (CTAB) as a cationic surfactant through a sol−gel autocombustion route. This route has an advantage over other studies involving sol−gel combustion, as the surfactant-based reaction keeps the sol particle separated because of the electrostatic stabilization. Sol−gel autocombustion is one of the cheapest methods with an advantage of lowering calcination temperature and production of ultra fine particles having large surface to volume ratio (15−19). Investigations on the variation of strain with size in CuO nanoparticles having different CTAB concentration in the precursor solution have been carried out. The samples without and with CTAB concentration were characterized by XRD, FESEM and TEM techniques. On the basis of the results obtained, the response of surfactant-assisted nanocrystalline CuO thick film toward ammonia gas at room temperature was also studied.

EXPERIMENTAL SECTION

$Cu(NO_3)_2.3H_2O$ and citric acid were used as starting materials. The precursor solution was prepared by taking metal nitrate to citric acid ratio 1:1. The pH of the solution was adjusted to 7 by adding liquid ammonia. In the first step, the solution was continuously stirred using a magnetic stirrer at 80°C for 4 h. An aqueous solution of CTAB ($(C_{16}H_{33})N(CH_3)_3Br$) was prepared by dissolving it in deionized water to give a final concentration of 0.01, 0.25, and 0.5 M. In the second step the 10 mL of aqueous CTAB solution was added to the precursor solution containing cupric nitrates with citric acid. The solution was thermally dehydrated in an oven (80 ± 5°C), which resulted in a viscous liquid. The viscous liquid was heated on a preheated hot plate maintained at a temperature around 300 °C. The material undergoes foaming followed by the decomposition of metal-citrate complex thus generating large volume of gases.

* Corresponding author. E-mail: iqbalsgh@yahoo.com. Phone: 91-9872828203. Fax: 91-183-2255619.

Received for review December 22, 2009 and accepted April 6, 2010

† Guru Nanak Dev University.

‡ Khalsa College.

DOI: 10.1021/am900914h

This results in a spontaneous ignition, undergoing combustion with flame, which results in enormous swelling and production of a blackish, foamy, voluminous mass in different fashion. The whole process was completed in less than 5−10 min in all cases. The voluminous and foamy products were easily crushed to get the decomposed gel. The detailed mechanism of the autocombustion reaction for metal nitrate to citric ratio 1:1 was discussed earlier (20). The decomposed gels so formed were calcined at 400 °C for 4 h with a heating rate of 10 °C/min in a muffle furnace (Macro Scientific). This results in a complete transformation to fine pure CuO powder without any impurity.

A known quantity of CuO powder was thoroughly mixed with few drops of diethnolamine and grinded in mortar and pestle to obtain a fine paste. The uniform layer of paste was deposited onto the glass slides, which were rinsed in nitric acid and then ultrasonically cleaned. The layer was dried at 400 °C in the muffle furnace for 1 h to burn out the organic binder. The thickness of the film was monitored using a depth profiler (Dektek 3030 XT) and was found to be 50 ± 5 μm.

The thermal analysis of the dried gel samples with and without the addition of surfactant was carried out using Perkin Elmer (Pyris diamond) thermal analyzer. The weight of the samples taken in both cases for thermal analysis were approximately 10.36 ± 0.15 mg. Air was used as purged gas in the analysis. The scan rate and air flow rate of 10 °C/min and 50 mL/min, respectively, were taken with alumina powder as a reference material. The phase identification of the decomposed gel and the calcined powders was performed by taking X-ray diffraction (XRD) pattern using X'Pert Panlytical diffractometer with Cu Kα radiation ($\lambda = 1.5405$ Å, 30 mA, 40 KV) in 2θ range 30−80°. The surface topography of copper oxide powder sample was studied by field emission scanning electron micrographs taken using JEOL JSM-6700F with a beam voltage of 30 kV. TEM images were taken using transmission electron microscope system (HRTEM, model FEI Technai 30) operated at 300 kV.

The electrical characterization of the film was done by heating with a specially designed heater and the temperature was measured using a K-type (chromel-alumel) thermocouple obtained from Omega Engineering Inc. (USA). The thick films were characterized for the response to ammonia gas in dc conductivity mode. The corresponding change in resistance was observed in the measuring cell made up of volume 500 cm^3 in the presence of air and ammonia gas atmosphere at room temperature (300 K) using Keithley 6517A electrometer having in built source of constant voltage power supply. Gas response of thick film sensor to ammonia is defined as the ratio of change in the resistance of the sample on exposure to ammonia to the resistance in air.

$$S = \frac{|R_g - R_a|}{R_a} \quad (1)$$

where R_g and R_a are CuO thick film resistance, measured in ammonia and air atmosphere, respectively. The time taken for the sensor to attain 90% of the maximum change in resistance on exposure to the target gas is the response time. The time taken by the sensor to get back 90% of the original resistance is the recovery time.

RESULTS AND DISCUSSION

Thermal Analysis. Observations show that the nitrate-citrate gel with metal nitrate to citric acid ratio 1:1 exhibit autocatalytic combustion behaviour. It is believed (14−19) that the exothermic heat generated in the combustion process is governed by a thermally induced redox reaction

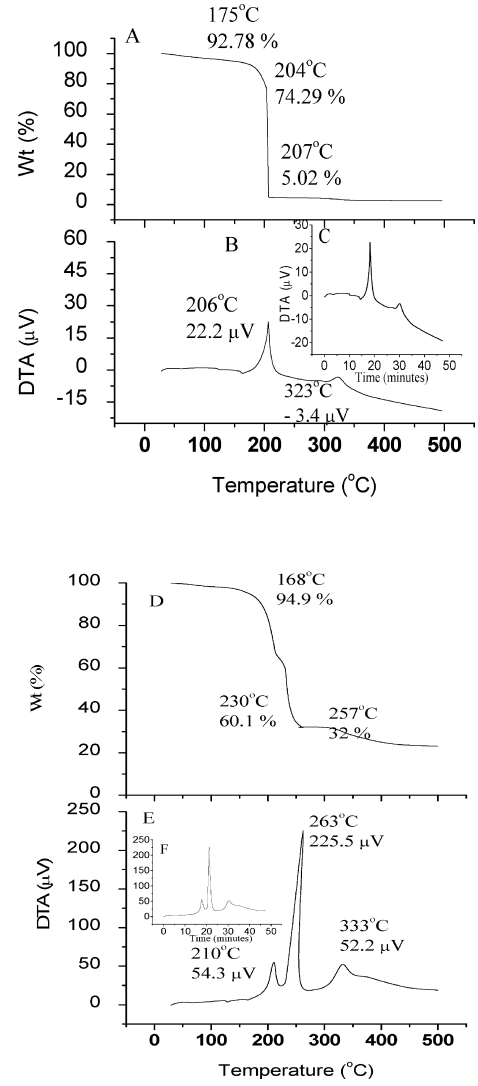

FIGURE 1. TG/DTA plots of the decomposed gels obtained (a−c) without CTAB and (d−f) with 0.5 M CTAB.

that involves the decomposition of the metal citrate complex formed in the precursor. Figure 1a−f shows the TGA/DTA plots of the metal−citrate complex decomposition by auto combustion reaction. The reaction mechanism can be formulated in terms of equation as follows

$$9Cu(NO_3)_2 + 5C_6H_8O_7 = 9\ CuO + 30CO_2 + 9N_2 + 20H_2O \quad (2)$$

The combustion rate was influenced by the addition of surfactant to the precursor solution. A gradual weight loss of 10% in TGA plots (Figure 1(a, d)) occurs in the temperature range 100−150°C, which is due to the removal of residual water in the gel. The exothermic behaviour of autoignition can be clearly seen in DTA curve in the temperature range 190−260°C with concurrent weight loss of 50−80% in the samples.

The weight loss has been observed to decrease from 90 to 72% when the surfactant concentration increases to 0.5 M in the solution. This may be attributed to the increase of

fuel content in the reaction mixture. The results indicate that the addition of 0.5 M CTAB increases the broadness of first exothermic peak and shift its position from 206 to 263 °C. The energy released from the reaction in case of surfactant assisted sample is comparatively higher in comparison to the sample without CTAB. The increase in the FWHM value of the exothermic peak from 7.53 to 10.14 °C clearly shows the sluggish nature of the reaction which leads to lower grain size and minimum agglomeration of oxide nanoparticles. The approximate time starting from the ignition of the reaction upto decomposition increases from 5 to 10 min with the addition of CTAB as shown in the inset of Figure 1(b, e). The second exothermic peak appeared in the DTA plot corresponds to the burning of residual organic matter and leave the system in the form of CO_x ($x = 1, 2$) gases. The peak shifts from 323°C to about 332°C with the addition of surfactant in the precursor solution. Huang et al. (21) has also reported the emission of CO_x ($x = 1, 2$) gases in the temperature range 220−420 °C for the synthesis of $BaFe_{12}O_{19}$.

The slow decomposition of the metal−citrate complex in addition to large exothermic heat produced in the reaction with the addition of surfactant helps to complete the combustion process, which leads to the completion of oxidation from Cu to CuO phase. The result shows that slow decomposition has an advantage over the fast decomposition of metal−citrate complex. The single-step decomposition provides insufficient time for the decomposition of the metal−citrate complex completely. The reaction ends up in minimum time, which leads to production of more undesirable phases of Cu in the decomposed gel such as metallic copper and Cu_2O. Investigations reveal that the surfactants are a potential source of heat and play a pivotal role as a fuel in addition to citric acid.

No significant weight loss has been observed beyond 400 °C before and after the addition of CTAB, as evident in the TGA curves thus indicate the thermal stabilization of the samples (20). On the basis of these observations, the optimum temperature for calcination of samples was chosen to be 400 °C.

XRD Analysis. The X-ray diffractograms of the decomposed gel with and without CTAB are illustrated in Figure 2. The diffraction peaks indicate the well ordered and nanosized copper oxide phases. The appearance of mixed phases has been supported by thermal analysis data, which suggests that insufficient heat and time makes the decomposition of metal−citrate complex incomplete. Intense diffraction peaks corresponding to reflection from (002) and (111) atomic planes of CuO phase have been found for the decomposed gel without and with different CTAB concentration at 2θ value 35.5 and 38.7°, respectively. In addition, a peak with lower intensity also appears corresponding to (111) atomic plane of Cu_2O at 2θ value 36.4°. With the increase in surfactant concentration, the intensity of the Cu_2O peak decreases, which may be attributed to the increased exothermic heat that probably cause the localized heating as

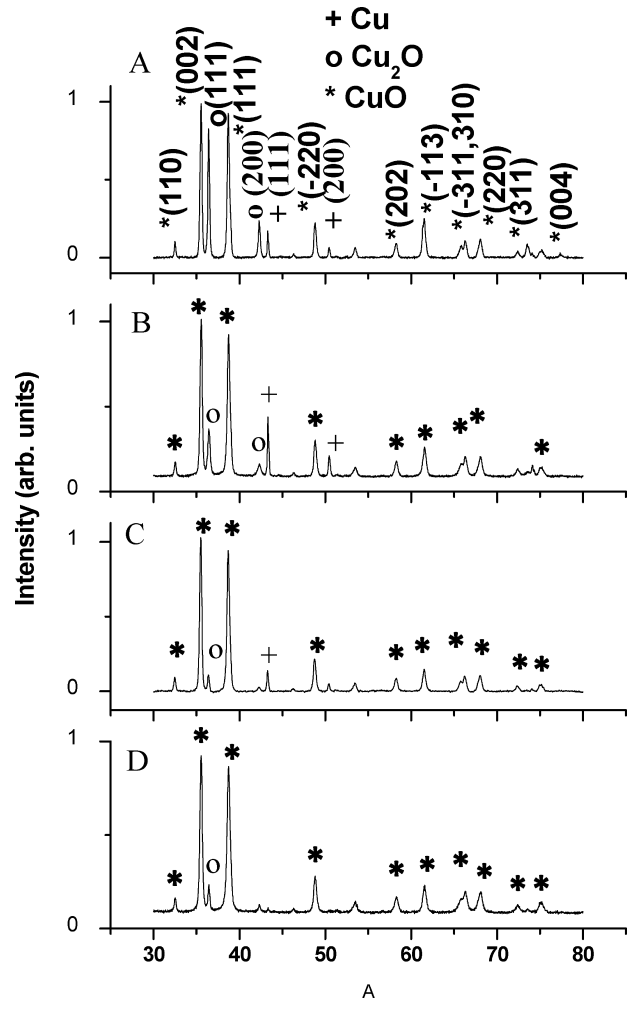

FIGURE 2. XRD pattern of the decomposed gel obtained (a) without CTAB and with (b) 0.01, (c) 0.25, and (d) 0.5 M CTAB addition.

well as enhanced temperature. This results in a nearly complete oxidation of metal ion.

The XRD diffractograms of the calcined samples without and with different CTAB concentration is shown in Figure 3. All the reflections on the pattern can be indexed as monoclinic CuO phase with peak positions corresponds to those reported by International Center for Diffraction Data (ICDD) card 41−254. The dominant peaks located at 2θ value 35.5 and 38.7° corresponds to reflection from (002) and (111) atomic planes, respectively, which indicates the existence of CuO phase. Interestingly, no peak corresponding to Cu_2O phase has been noticed in the diffraction pattern of calcined samples, thus indicating complete transformation to the CuO phase.

The observed d value of the calcined samples with and without CTAB shift to lower and higher sides, respectively, when compared to the d value as reported by the ICDD card of CuO. This suggests the accumulation of compressive strain in the case of surfactant-assisted CuO, although tensile strain is observed in the case of the sample without CTAB. These observations are in agreement with those reported by Ramgir et al. (22). The average grain size and the internal lattice strain of the calcined samples have been evaluated by the Hall−Williamson equation expressed as (23)

$$\frac{\beta\cos\theta}{\lambda} = \frac{1}{D} + \frac{\varepsilon\sin\theta}{\lambda} \quad (3)$$

where β is the FWHM of the powder, θ the Bragg angle, λ the wavelength of X-ray used, D the crystallite size, and ε the internal strain. The D and ε values of the samples were calculated from the least square fit to $(\beta\cos\theta)/(\lambda)$ vs $(\sin\theta)/(\lambda)$ plots for the prominent peaks having comparatively higher intensity as shown in Figure 4. It has been observed that the addition of CTAB in the reaction mixture results in a decrease in the average crystallite size. The crystallite size of around 18 nm has been observed in case of the CuO with 0.5 M CTAB, thus indicating the formation of nanocrystalline CuO phase. A negative and positive slope of the plots observed in case of CuO samples with and without CTAB confirms the presence of compressive and tensile strain in the crystal lattice (24). The higher magnitude of the slope with the incorporation of CTAB in CuO suggests the enhancement of the strain with the reduction in crystallite size. The lattice parameters ($a \neq b \neq c$, $\alpha = \gamma = 90° \neq \beta$ for monoclinic structure) and the volume of the unit cell have been calculated using the relations

$$\frac{1}{d^2} = \frac{1}{\sin^2\beta}\left(\frac{h^2}{a^2} + \frac{k^2\sin^2\beta}{b^2} + \frac{l^2}{c^2} - \frac{2hl\cos\beta}{ac}\right) \quad (4)$$

$$V = abc\sin\beta \quad (5)$$

where d is the interplanar spacing, h, k, l are Miller indices of the crystal planes, a, b, c, β are the lattice parameters and V is the volume of the unit cell. The values of the lattice parameters with estimated error are recorded in Table 1 and found to be in good agreement with those contained in ICDD card. Investigations reveal that the CTAB addition in CuO causes a decrease in the crystallite size and an increase in the unit-cell volume. The overall effect of CTAB addition is to generate a nonuniform strain in the nanocrystallites. Similar results have also been obtained in the case of Ru-doped SnO_2 by Niranjan et al. (24) and ZnSe films by Mazher et al. (25).

FESEM and TEM Analysis. The FESEM images of the CuO samples calcined at 400°C with and without CTAB are shown in Figure 5. The porous feature of the agglomerates obtained in all the samples may be attributed to the liberation of large amount of gas during combustion. The particles appear to bound together into agglomerates of different shapes and sizes. The agglomerates in the sample without surfactant show comparatively dense structure with distorted spherical shape. The shape of the particles improves and approaches spherical morphology with the increase in concentration of CTAB as shown in the Figure 5(b-d). The

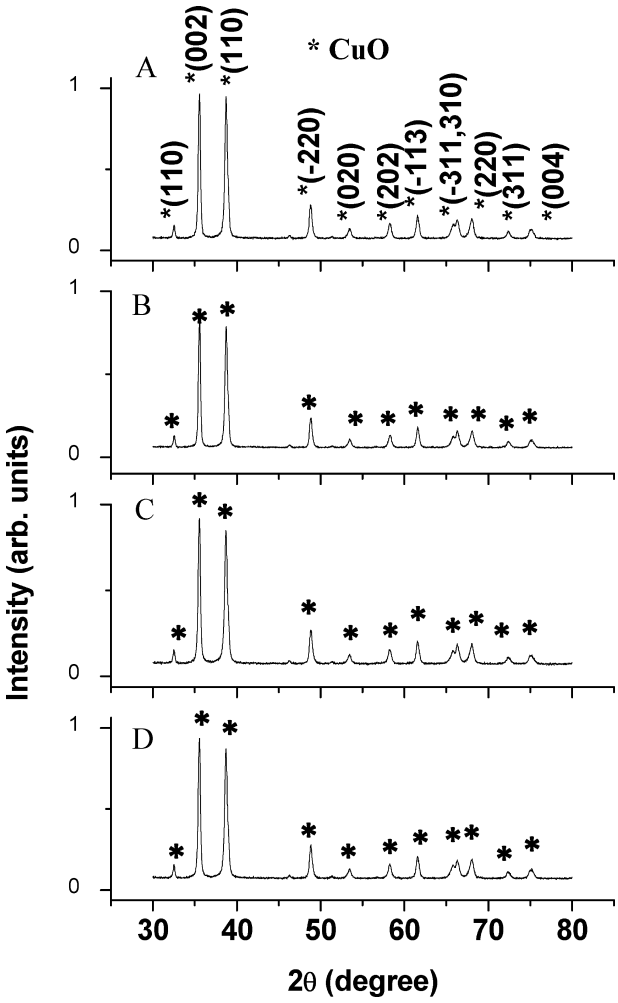

FIGURE 3. XRD pattern of the samples calcined at 400°C (a) without CTAB and with (b) 0.01, (c) 0.25, and (d) 0.5 M CTAB addition.

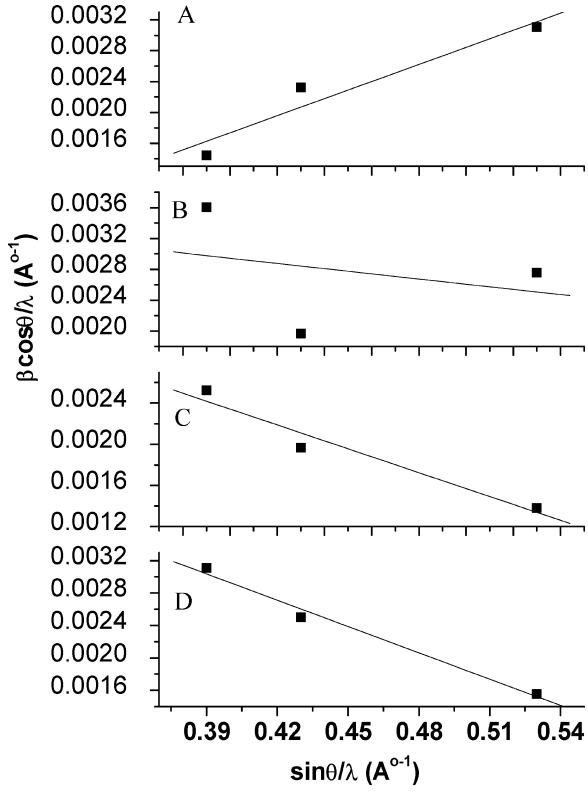

FIGURE 4. Plot of Hall equation for the samples calcined at 400°C (a) without CTAB and with (b) 0.01, (c) 0.25, and (d) 0.5 M CTAB addition.

Table 1. Values of the Lattice Constant, Parameters, Crystallite Size Calculated Using Hall Equation, Crystallite Size from TEM Measurements, Activation Energy, and Response Calculated from the Electrical Characterization for the Samples Calcined at 400 °C without and with Different Concentrations of CTAB

	without CTAB	0.01 M CTAB	0.25 M CTAB	0.5 M CTAB
a (Å)	4.682 (0.0003)	4.676 (0.0016)	4.682 (0.0003)	4.698 (0.0030)
b (Å)	3.424 (0.0004)	3.427 (0.0012)	3.427 (0.0012)	3.425 (0.0007)
c (Å)	5.114 (0.0028)	5.114 (0.0028)	5.115 (0.0026)	5.116 (0.0024)
β (deg)	99.111 (0.0043)	99.282 (0.0025)	99.070 (0.0026)	99.278 (0.0026)
cell volume (Å^3)	80.949 (0.0044)	80.877 (0.0045)	81.045 (0.0041)	81.242 (0.0038)
d_{obsd} (Å) (type of strain)	2.5251 (tensile)	2.5239 (compressive)	2.5230 (compressive)	2.5228 (compressive)
nonuniform strain (ϵ)	0.0026	−0.0007	−0.003	−0.006
average crystallite size (nm) XRD (standard deviation)	100 (28)	41 (12)	25 (10)	18 (11)
average crystallite size (nm) TEM	70	30	25	7
activation energy (eV) E_1	0.222	0.203	0.345	0.542
T_1 (K)	303−473	303−378	303−353	303−353
activation energy (eV) E_2		0.401	0.259	0.286
T_2 (K)		378−473	353−473	353−473
response (S)	−0.81	−0.88	−0.95	−9.83

[a] Minus sign with the response means that the sensor's resistance decreases during the gas hit.

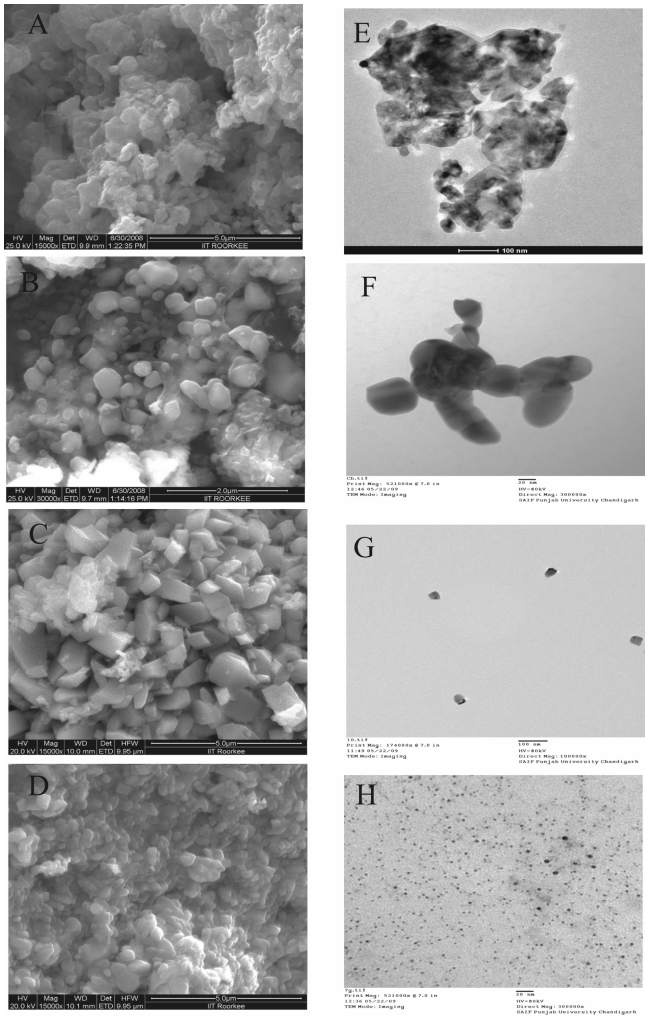

FIGURE 5. (a−d) FESEM and (e−h) TEM micrographs of the sample without surfactant and with 0.01, 0.25, and 0.5 M CTAB, respectively.

particle size of the CTAB surfactant assisted samples lie in the range 20−30 nm, while samples without surfactant shows comparatively large particle size around 125 nm. The increase in concentration of surfactant appears to decrease the size of particle. These observations are in conformity with the reported results for CTAB assisted growth of strontium hexaferrite nanopowder (14).

The variation in the shape and size of the CuO nanoparticles is in fact the consequence of the reaction conditions during the powder preparation. The particle size and the agglomeration in the material depend mainly on the way the combustion propagates and the amount of disintegration occurs. In the case of the reaction mixture with a 1:1 MN:CA ratio, the reaction proceeds at faster propagation rate with a high flame temperature generated during combustion as compared to the fuel enriched conditions. The high flame temperature associated with the stoichiometric reaction may result in the local calcination among the primary formed particle. Consequently, the particles grow as the reaction propagates even during the post thermal treatment applied to remove the organics. The decrease in agglomeration of the particles as observed in Figure 5b−d may be assigned to the addition of CTAB in reaction mixture, which is a source of carbon and acts as a fuel as evident from the thermal analysis data. The addition of CTAB increases the content of fuel, which forced the reaction to proceed slowly and with increased exothermicity. Especially the excess fuel may act as a space filling agent, which will leave empty spaces as fuel burns during the reaction and thus result in the existence of huge porosity of the product. Increasing the fuel content would further cause more gas liberation, which helps to disintegrate the agglomerates into nanoparticles and reduce their subsequent growth. Similar results have also been discussed during the synthesis of $LiMn_2O_4$ and Ni-YSZ cerment electrodes by combustion synthesis by Kovacheva et al. (26) and Marjan et al. (27).

TEM images of the CuO samples with CTAB show the porous nature and minimum agglomeration with spherical-shaped particles as shown in Figure 5f−h. The crystallite size distribution for the sample without CTAB is found to be broader, whereas CTAB addition reduces the crystallite size

as well as brings the distribution in a narrow range of 5−10 nm as recorded in the Table 1. The spherical nature of the CuO crystallites appearing in TEM images for the samples prepared with CTAB may be attributed to the formation of spherical micelles in the gel. Hasab et al. (14) also demonstrated that the micelles in the gel control the growth of crystallites as well as agglomeration.

Electrical Characterization. The electrical resistance of the film was measured as function of temperature in the range 300−473 K. The resistance of the film determined at room temperature increases from 3.41 to 20.40 MΩ when CTAB concentration increases from zero to 0.5 M. The decrease in resistance of film with temperature is quite likely as large number of oxygen molecules are chemisorbed at the grain boundary and on the surface of the film. It may be mentioned that the principal chemisorption species in CuO is O_2^{-1} at room temperature (28). With the rise in temperature, the rate of chemisorbtion of O_2^{-1} increases on the sample surface, which results in the decreasing of the surface resistance of films. The dependence of conductivity on temperature can be represented by the Arrhenius equation (29)

$$\sigma = \sigma_0 \exp\left(-\frac{\Delta E_a}{kT}\right) \quad (6)$$

where ΔE_a is the activation energy that corresponds to the energy difference between the valence band and the conduction band, σ_o is a temperature independent factor, and K is the Boltzman's constant, and T is the absolute temperature. The increase in conductivity of the films with temperature indicate their semiconductive behaviour. Figure 6. depicts the lnσ vs. 1000/T plots for CuO samples without and with surfactant of different concentrations. The linear nature of the plots indicates that the themoionic emission plays a major role in the carrier transport with in the experimental temperature range (30). The activation energies of the samples have been obtained from the slope of plots and are given in the Table 1. Observations reveal that more than one activation energy E_1 and E_2 corresponding to temperature ranges T_1 and T_2, respectively, of the charge carriers exists in case of surfactant-assisted CuO samples. The value of activation energy found to be 0.222 eV in the case of CuO sample without CTAB, whereas it increases to 0.542 and 0.286 eV, corresponding to the temperature ranges 303−353 and 353−473 K, respectively, with the addition of 0.5 M surfactant solution. The increase of activation energy of CTAB assisted samples can be understood from the decrease in crystallite size as confirmed by XRD and TEM analysis. The decrease in crystallite size increases the scattering of carriers at grain boundaries, and thus results in a decrease in the mobility as suggested by Bouderbala et al. (31). The porous nature of the CuO nanocrystallites might also be responsible for the increases in resistance and hence activation energy. Perez-Ramos et al. (32) have also observed the effect of porosity on the electrical conductivity in the case of Fe-based samples.

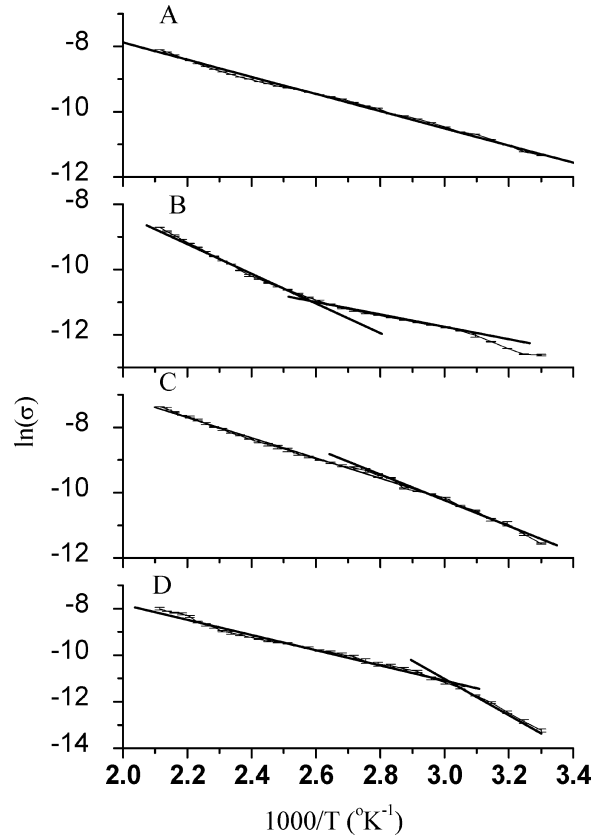

FIGURE 6. Ln(σ) vs 1000/T plot for the samples calcined at 400 °C (a) without CTAB and with (b) 0.01, (c) 0.25, and (d) 0.5 M CTAB addition.

Ammonia Response. The response characteristics of CuO thick films prepared with and without CTAB exposed to 100 ppm of ammonia gas are shown in the Figure 7. A decrease in surface resistance of the film has been observed with the introduction of ammonia. This may be assigned to the redox reaction of ammonia with the adsorbed oxygen species O_2^-. It can be seen that CuO thick film sensor have good sensing performance with high sensitivity and a short response time. The response of the sensor for ammonia increases to 9.83 with the addition of 0.5M CTAB surfactant. The higher response in case of sensor with CTAB may be attributed to the small crystallite size and huge porosity in the material as suggested by Jimenez et al. (33). Similar results have been obtained for the barium strontium titanate thick film sensor for ammonia by Jain et al. (34). The recovery time of the sensor without CTAB is about 58% in 500 s, whereas with the addition of 0.5M CTAB it raises to 88% in the same time. It can be seen that the recovery time in the thick film sensor of CuO with and without CTAB is larger possibly because of the formation of NO_2 as a result of the redox reaction of ammonia which is hardly to desorb at room temperature.

Sensing Mechanism. Gas molecules are adsorbed on active sites of the metal oxide surface, where their bonds weakened or broken have obvious tuning effects on the electrical properties of the CuO nanoparticles. On exposure to ambient air, oxygen molecules absorb on the surface of the nanoparticles and affect the carrier density. The surface

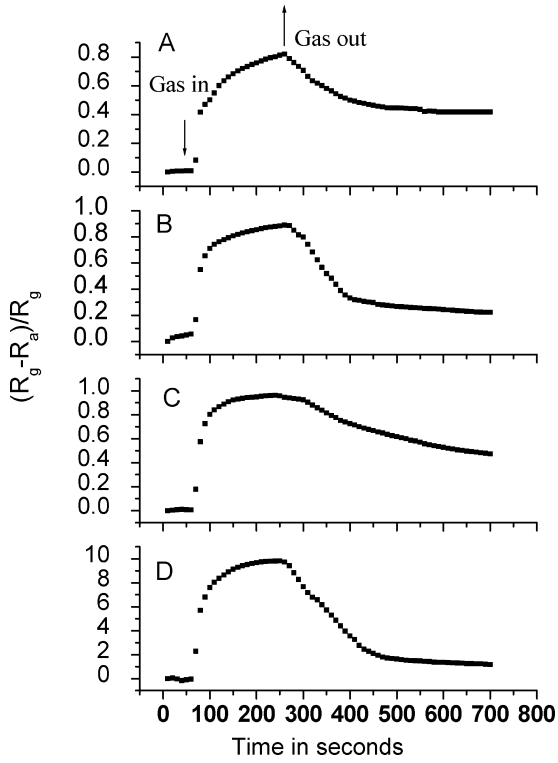

FIGURE 7. Response of CuO thick films for ammonia at room temperature for the samples calcined at 400°C (a) without CTAB and with (b) 0.01, (c) 0.25, and (d) 0.5 M CTAB addition.

of nanocomposite is sensitive to both oxidizing and reducing analytes due to the presence of adsorbed oxygen species on the outer layer of the nanoparticles. The oxygen is adsorbed on the oxide surface as different species. At room temperature predominant surface oxygen species O_2^- is most active one (34).

$$O_2(g) = O_2(ad) \quad (7)$$

$$O_2(ad) + e^- = O_2^-(ad) \quad (8)$$

Intermediate adsorbed species formed react with oxygen species leading to a change in the height of the intergrain potential barrier. If the oxide is p-type semiconductor, the adsorption of oxygen enhances the carrier (hole) concentration on the surface and the resistance decreases due to lowering of potential barrier. When gas comes in contact with such oxygen species covering the oxide surface, the reaction between the gas and adsorbed oxygen changes the charge carrier concentration. Therefore the conductivity will vary in the presence of the gas. When the gas was removed, the formed products desorbed, leaving the active sites for further reaction.

In the field of catalyst and gas sensing three competitive reactions have been proposed for ammonia oxidation on metal oxide (33, 34).

$$2NH_3 + 3(O) = N_2 + 3H_2O + 6e^- \quad (9)$$

$$2NH_3 + 4(O) = N_2O + 3H_2O + 8e^- \quad (10)$$

$$2NH_3 + 5(O) = 2NO + 3H_2O + 10e^- \quad (11)$$

where (O) is oxide in regular oxygen sites, and it can be substituted by the appropriate amounts of chemisorbed O^- or O_2^- species. All the oxygen consuming processes raise the conductance of the metal oxide layer. The reactions show that many intermediate species and more reaction routes are involved. All factors may differently affect the response of sensor. The sensor response of pure CuO to ammonia was interfered with the presence of NO_x, a product of ammonia oxidation, which causes an opposite change in resistance of the film when exposed to ammonia.

The electron-donor gas and electron-acceptor gas induces opposite effect on the electrical transport of a p-type semiconductor. As a consequence, electrons are transferred to NH_3 molecules from the valence band of the CuO, increasing the density of holes, thereby decreasing the electrical resistance. Similar results have been observed by Liao et al. (35) for p type semiconductive mesoporous carbon nanofibres when exposed to NO_2 gas.

Though the gas sensor based on a CTAB-assisted CuO thick film shows a comparatively better response toward NH_3 at room temperature as compared to the CuO sensor tested by Alexy et al. (36), it is interesting to reveal that the ammonia gas sensor based on CuO shows a much better response at room temperature in comparison to n-type materials like ZnO and SnO_2 at 100°C (3). However, the longer recovery time due to the slow rate of desorption is the main drawback. More detailed investigations have to be performed in this regard. In future work, we will go on searching the materials added to CuO and solving the problem for application.

CONCLUSION

A nanocrystalline CuO powder was synthesized by a surfactant assisted sol–gel autocombustion method. It has been shown that the crystallite size of CuO powder can be controlled by adding cationic surfactant in the reaction mixture. The spherical CuO nanocrystallites of size around 18 nm and with minimum agglomeration were obtained with 0.5M CTAB concentration. The activation energy of CuO appears to be enhanced with an increase in surfactant concentration. Interestingly, an enhancement in the response of around 12 times for 0.5 M CTAB-assisted CuO sensor toward ammonia at room temperature has been recorded when compared to sensor without the addition of surfactant. Observation also reveals that the synthesized CuO sensors show a comparatively better response to those reported for n-type metal oxide films.

Acknowledgment. The authors thank Director Indian Institute of Technology Roorkee, Sophisticated Test & Instrumentation Centre, Kochi and Central Instrumentation

Laboratory, Panjab University, Chandigarh, for providing FESEM, EDAX, and XRD facilities.

REFERENCES AND NOTES

(1) Dmitriev, S.; Lilach, Y.; Button, B.; Moskovits, M.; Kolmakov, A. *Nanotechnol.* **2007**, *18*, 055707.
(2) Rumyantseva, M. N.; Kovalenko, V. V.; Gaskov, A. M.; Pagnier, T. *Russ. J. Gen. Chem.* **2008**, *78*, 1081.
(3) Rout, C. S.; Hegde, M.; Govindaraj, A.; Rao, C. N. R. *Nanotechnology* **2007**, *18*, 205504(1−9).
(4) Timmer, B.; Olthuis, W.; Berg, A. *Sens. Actuators, B* **2005**, *107*, 666.
(5) Lee, J. H. *Sens. Actuators, B* **2009**, *140*, 319.
(6) Sukhorukov, Y. P.; Gizhevskii, B.A.; Mostovshchikova, E.V.; Yermakov, A. Ye.; Tugushev, S. N.; Kozlov, E. A. *Tech. Phys. Lett* **2006**, *32*, 132.
(7) Zhu, Y. W.; Yu, T.; Cheong, F. C.; Xu, X. J.; Lim, C. T.; Tan, V. B. C.; Thong, J. T. L.; Sow, C. H. *Nanotechnology* **2005**, *16*, 88.
(8) Zhou, K.; Wang, R.; Xu, B.; Li, Y. *Nanotechnol.* **2006**, *17*, 3939.
(9) Zhang, J.; Liu, J.; Peng, Q.; Wang, X.; Li, Y. *Chem. Mater.* **2006**, *18*, 867.
(10) Liu, Q.; Liang, Y.; Liu, H.; Hong, J.; Xu, Z. *Mater. Chem. Phys.* **2006**, *98*, 519.
(11) Liu, B. H.; Zeng, C. *J. Am. Chem. Soc.* **2004**, *126*, 8124.
(12) Kida, T.; Oka, T.; Nagano, M. *J. Am. Cerm. Soc.* **2007**, *90* (1), 107.
(13) Chen, D.; Shen, G. Z.G.; Tang, K.; Qian, Y. *J. Cryst. Growth* **2003**, *254*, 225.
(14) Hasab, M. G.; Ebrahimi, S. A. S.; Badiei, A. *J. Eur. Ceram. Soc.* **2007**, *27*, 3637.
(15) Alamolhoda, S.; Seyyed Ebrahimi, S. A.; Badiei, A. *J. Magn. Mater.* **2006**, *303*, 69.
(16) Zhou, J.; Wang, Y.; Zhao, F.; Wang, Y.; Zhang, Y.; Yang, L. *J. Lumin.* **2006**, *119*, 248.
(17) Hiremath, V. A.; Venkataraman, A. *Bull. Mater. Sci.* **2003**, *26*, 391.
(18) Kikkawa, S. *J. Am. Ceram. Soc.* **2005**, *88* (2), 308.
(19) Lagashetty, A.; Venkataraman, A. *Bull. Mater. Sci.* **2004**, *27*, 491.
(20) Bedi, R. K.; Singh, I. *Curr. Nanosci.* **2009**, *5*, 3–273.
(21) Huang, J.; Zhuang, H.; Li, W. *Mater. Res. Bull.* **2003**, *38*, 149.
(22) Ramgir, N. S.; Hwang, Y. K.; Mulla, I. S.; Chang, J. *Solid State Sci.* **2006**, *8*, 359.
(23) Williamson, G. K.; Hall, W. H. *Acta Mater.* **1953**, *1*, 22.
(24) Niranjan, R. S.; Hwang, Y. K.; Kim, D. K.; Jhung, S. H.; Chang, J. S.; Mulla, I. S. *Mater. Chem. Phys.* **2005**, *92*, 384.
(25) Mazher, J.; Shrivastav, A. K.; Nandedkar, R. V.; Panday, R. K. *Nanotechnology* **2004**, *15*, 572.
(26) Kovacheva, D.; Godjov, H.; Petrov, K.; Mandal, S.; Lazarraga, M. G.; Pascural, L.; Amarilla, J. M.; Rojas, R. M.; Herrero, P.; Rojo, J. M. *J. Mater. Chem.* **2002**, *12*, 1184.
(27) Marjan, M.; Klementina, Z.; Jadran, M. *J. Power Sources* **2002**, *106*, 178.
(28) Park, C. O.; Akbar, S. A. *J. Mater. Sci.* **2008**, *38*, 4611.
(29) Hakim, A.; Hossain, J.; Khan, K. A. *Renewable Energy* **2009**, *34*, 2625.
(30) Devan, R. S.; Kolekar, Y. D.; Chougule, B. K. *J. Phys.: Condens. Mater.* **2006**, *18*, 9809.
(31) Bouderbala, M.; Hamzaoui, S.; Adnane, M.; Sahraoui, T.; Zerdali, M. *Thin Solid Film* **2009**, *517* (5)), 1572.
(32) Perez- Ramos, M. E.; Manzano-Ramirez, A.; Vorobiev, P. Yu.; Horiey, P. P.; Vorobiev, Yu. V.; Gonzalez-Hernandez, J. *Inorg. Mater.* **2003**, *39*, 37.
(33) Jimenez, I.; Centeno, M. A.; Scotti, R.; Morazzoni, F.; Arbiol, J.; Cornet, A.; Morante, J. R. *J. Mater. Chem.* **2004**, *14*, 2412.
(34) Jain, G. H.; Patil, L. A.; Patil, P. P.; Mulik, U. P.; Patil, K. R. *Bull. Mater. Sci.* **2007**, *30* (1)), 9.
(35) Liao, L.; Zheng, M.; Zhang, Z.; Yan, B.; Chang, X.; Ji, G.; Shen, Z.; Wu, T.; Cao, J.; Zhang, J.; Gong, H.; Cao, J.; Yu, T. *Carbon* **2009**, *47*, 1841.
(36) Alexey, A.T.; Gregory, P.H.; Brent, T.M.; John, W.A. *Sens. Actuators, B* **2003**, 93126.

AM900914H